ENGINEERING

Magnetically levitated metasurface enabling tangible and bidirectional human-machine interaction

Gooyoon Chung[1]†, Jeongmin Yoo[1]†, Pei Liu[2]†, Gyuri Shin[1], Dongkyu Jeong[1], Sunjin Lee[1], Jae-Young Yoo[3], Sang Min Won[4], Dong-Soo Han[5], Ji-Hoon Kim[6,7], Wooseok Song[8], Raudel Avila[2]*, Yoonseok Park[1]*

Mechanical metasurfaces are deformable surfaces that reconfigure their shape in response to external stimuli, with growing applications in interactive displays and human-machine interfaces. However, many existing systems are either too fragile for physical interaction or too slow to match human response. Moreover, their incompatibility for integrating functional systems constrains seamless interaction with humans. We developed a robust, rapidly responsive, and multifunctional soft metasurface capable of intuitive interaction with humans. The soft surface reconfigures through magnetic actuation, enabling mechanical metasurface functions with simultaneous visual and tactile feedback for human interaction. The system features a six-by-six array of elastomeric pixels, each actuated by attractive or repulsive magnetic forces from an underlying electromagnet array. The induced magnetic force modulates the surface height up to 8.5 millimeters (−5 to 3.5 millimeters), enabling coordinated actuation of 36 electromagnets to reconstruct over 10^{30} discrete surface morphologies. Its mechanics compliant design allows human interaction such as pushing, pulling, and pinching. Embedded inertial measurement unit sensors reconstruct surface shape in real time, and an integrated light-emitting diode array provides immediate visual feedback. This platform enables fast, reversible, and intuitive interaction between users and programmable surfaces, laying the groundwork for next-generation human-machine interaction systems.

INTRODUCTION

Mechanical metasurfaces, defined as deformable surfaces capable of actively morphing their geometry in response to external stimuli, are attracting growing interest in interactive technologies, tactile interfaces, and bioinspired systems (*1*–*3*). These surfaces can encode, communicate, and process information through physical deformation, offering unexpolored modalities for dynamic information transfer and human-machine interaction (*4*). Advances in soft materials and remote actuation strategies have enabled a range of programmable surfaces (*5*–*7*). However, most implementations remain impractical for real-world interaction due to structural and functional limitations. A wide variety of mechanical metasurfaces have been demonstrated using pneumatic actuators (*8*–*11*), dielectric elastomers (*12*–*14*), magnetic composites (*15*, *16*), liquid crystal elastomers (*17*, *18*), shape memory materials (*19*, *20*), and liquid metals (*21*–*23*).

While these platforms exhibit diverse shape transformations, they typically suffer from three key drawbacks. First, many systems are either too fragile or too rigid to accommodate physical interaction. Structures made from thin films or microscale elements are often so compliant that they deform permanently under external mechanical loads and stimulation, leading to functional failure (*24*, *25*). On the other hand, rigid systems designed for structural stability are too stiff to respond to mechanically intricate user input, such as pinching and twisting (*11*, *13*–*20*). In both cases, the lack of interactive compliance limits their suitability for human-machine interfaces. Second, systems that use joule heating or ion migration as their actuation mechanism suffer from inherently slow response times due to thermal diffusion or charge accumulation limits (*17*–*20*, *25*). These constraints prevent rapid, continuous shape adaptation, resulting in a mismatch with human spatiotemporal responses and limiting dynamic human-machine interaction. Third, most mechanical metasurfaces face challenges in directly integrating multiple sensors and actuators onto their surfaces, limiting real-time shape sensing (*8*, *18*–*21*). Surface deformation is typically monitored using external devices such as depth cameras, which increase system complexity and fail to operate during direct physical interaction, hindering real-time feedback and control (*23*–*25*).

To overcome these challenges, we present a magnetically actuated soft mechanical metasurface that integrates programmable shape morphing, embedded self-sensing, and real-time visual feedback in a fully soft and magnetically levitated platform. Our system features a layered elastomeric structure embedded with composite magnets that locally deform in response to attractive and repulsive magnetic forces generated by a pixelated electromagnet array. A dual-layer configuration, with actuating magnets (AMs) and supporting magnets (SMs), enables independent upward and downward displacement. Magnet dimensions and mixing ratios are optimized for stable and reversible actuation.

To enable autonomous surface monitoring, we embed inertial measurement unit (IMU) sensors within the actuating layer. These sensors allow real-time reconstruction of the surface shape without the need for external imaging equipment and remain functional during direct physical contact such as pressing or pinching. Furthermore, we integrate an array of light-emitting diodes (LEDs) onto the surface,

[1]Department of Materials Science and Engineering, Kyung Hee University, Yongin 17104, Republic of Korea. [2]Department of Mechanical Engineering, Rice University, Houston, TX 77005, USA. [3]Department of Semiconductor Convergence Engineering, Sungkyunkwan University, Suwon 16419, Republic of Korea. [4]Department of Electrical and Computer Engineering, Sungkyunkwan University, Suwon 16419, Republic of Korea. [5]Center for Spintronics, Korea Institute of Science and Technology, Seoul 02792 Republic of Korea. [6]Molecular Recognition Research Center, Korea Institute of Science and Technology, Seoul, Republic of Korea. [7]KHU-KIST Department of Converging Science and Technology, Kyung Hee University, Seoul 02447 Republic of Korea. [8]Korea Research Institute of Chemical Technology (KRICT), Daejeon 34114, Republic of Korea.
*Corresponding author. Email: ra88@rice.edu (R.A.); yoonseok.park@khu.ac.kr (Y.P.)
†These authors contributed equally to this work.

mapping sensor-derived height data to color gradients in real time. As a result, the metasurface functions as a dynamic three-dimensional (3D) display that both deforms and visually communicates its shape. An overview of the system configuration, shape-morphing behavior, and potential applications is illustrated in Fig. 1, which highlights the integration of actuation, sensing, and visual feedback in a single platform. Through this combination of shape adaptation, sensing, and visual output, our system mimics key characteristics of biological surfaces. It responds to external stimuli by changing its physical form, detects mechanical deformation with embedded sensors, and expresses its internal state through visual cues. By replicating wave-like and ripple motions along with corresponding color changes, the metasurface demonstrates bioinspired capabilities in both behavior and appearance.

This work introduces a mechanically soft metasurface that seamlessly integrates magnetic actuation, embedded sensing, and surface-level visual feedback. The system tolerates and recovers from direct human interaction, including pinching and twisting. This multifunctional platform establishes a foundation for programmable, responsive, and human-interactive surfaces for next-generation tactile interfaces and bioinspired display technologies.

RESULTS

Composition and operating mechanism of the metasurface

Figure 2A presents the exploded view of the 6 by 6 metasurface, which consists of three primary layers arranged from top to bottom: the actuating layer, supporting layer, and electromagnet array. We fabricate the actuating layer using soft elastomer (Ecoflex 00-30; Young's modulus, 100 kPa) and embed AMs into each of the 36 pixels. A supporting layer composed of a stiffer elastomer (Dragon Skin 30; Young's modulus, 240 kPa) is placed underneath, with SMs aligned beneath each pixel. At the bottom, the electromagnet array actively controls each pixel's height through magnetic interactions. We fabricate both AMs and SMs using composites of polydimethylsiloxane (PDMS) and neodymium-iron-boron (NdFeB) microparticles (MPs) but applied different geometries and mixing ratios depending on their functional roles. The AMs have a radius of 6 mm and a height of 3 mm and contain 75 wt % MPs, whereas the SMs have a radius of 7 mm and a height of 1 mm and contain 50 wt % MPs. The fabricated PDMS-NdFeB composite exhibits excellent mechanical stability under repeated deformation (*26*, *27*).

To illustrate the operating principle, Fig. 2B shows the behavior of a single pixel under three magnetic conditions: no field, repulsion, and attraction. In the absence of an external magnetic field, the AM and SM face each other with the same magnetic orientation, generating a repulsive force that induces a small upward displacement in the actuating layer. When a repulsive magnetic field is applied to the AM, it displaces upward, while the SM moves downward, increasing their distance and weakening the interaction. Under an attractive field, the AM moves downward and the SM upward, resulting in coupled motion. Effective downward displacement requires the attractive force on the AM to exceed the repulsive force from the SM.

Following this principle, we optimized the geometry and magnetic properties of the AMs to maximize upward displacement. Achieving this goal requires a strong magnetic force and low mass design. We tested AMs with radii of 5, 6, and 7 mm and heights of 2 and 3 mm

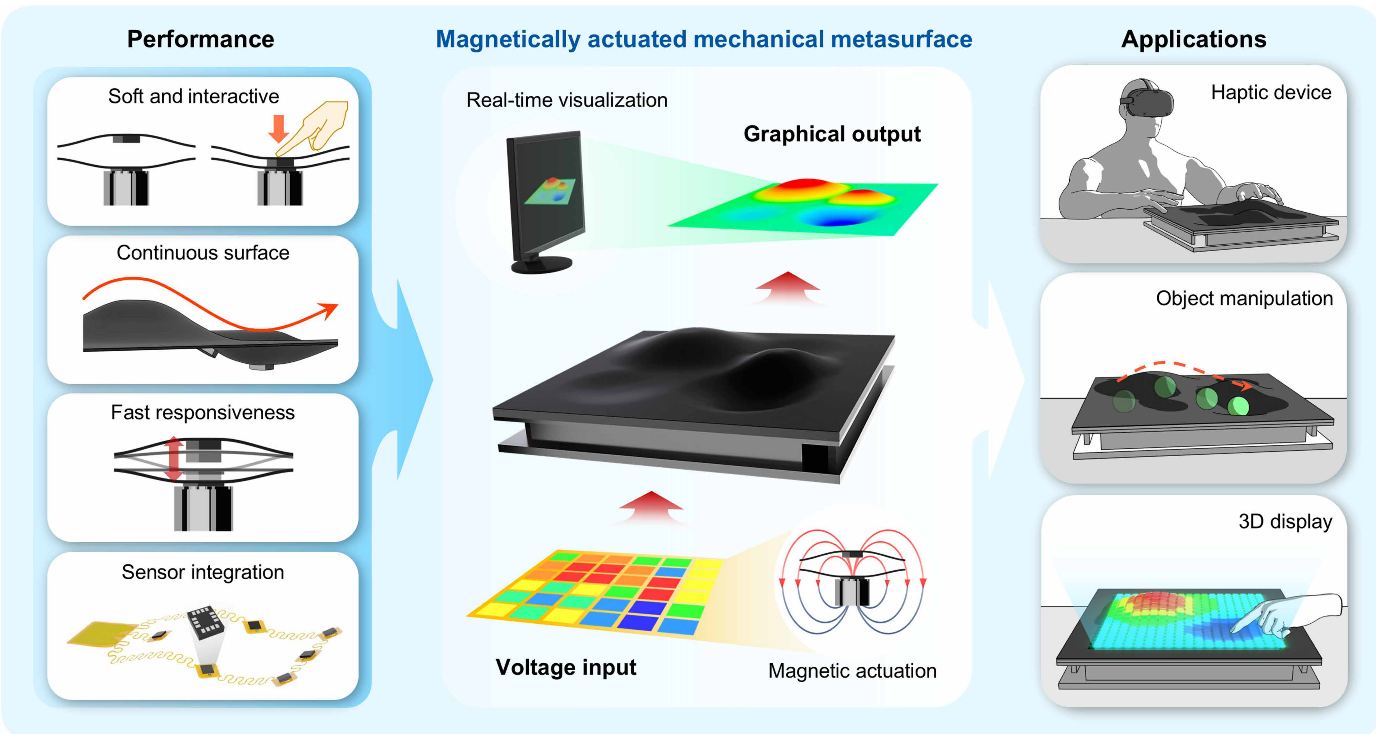

Fig. 1. Overview of the magnetically actuated soft mechanical metasurface. Schematic illustration of the metasurface architecture, its shape-morphing capability, and potential applications in interactive sensing and display systems. (Created using Blender by G.C., J.Y., and Y.P., Kyung Hee University.)

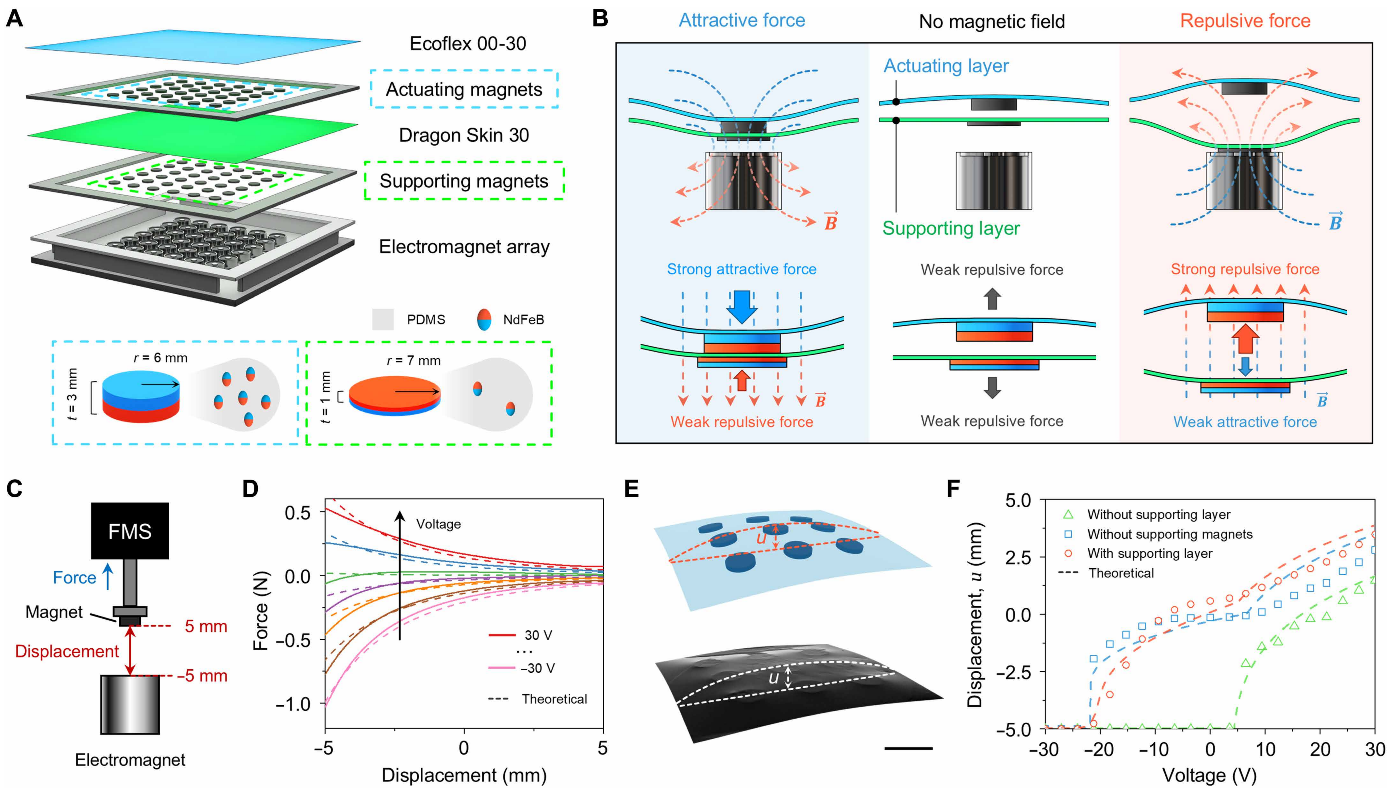

Fig. 2. Structural design and magnetic interaction mechanism of the metasurface. (**A**) Exploded view of the 6 by 6 metasurface showing the layered configuration of Ecoflex 00-30, AMs, Dragon Skin 30, SMs, and the electromagnet array. (**B**) Working principle of a single pixel under no field, repulsive, and attractive magnetic configurations. (**C**) Setup for measuring magnetic interaction force using a force measurement system (FMS). (**D**) Measured magnetic force between the electromagnet and AM as a function of displacement and polarity. (**E**) Photograph of the central pixel during actuation and definition of displacement. Scale bar, 20 mm. (**F**) Comparison of displacement responses under three supporting layer configurations: without supporting layer, without SMs, and with SMs. (Created using Blender by G.C., J.Y., and Y.P., Kyung Hee University.)

by measuring their weight and surface magnetic flux density. The results showed that thicker magnets exhibited stronger magnetic flux, while larger volumes increased weight, indicating a trade-off between magnetic performance and mass (fig. S2).

To evaluate the vertical actuation performance, we directly measure the interaction force between the AM and the electromagnet under different conditions. Figure 2C shows the experimental setup. We vary the voltage applied to the electromagnet and quantified the attractive and repulsive forces exerted on the AM. As shown in fig. S3, increasing the mixing ratio or thickness of MPs enhances the interaction force, and the AM with a radius of 6 mm generates the strongest response. On the basis of these findings, we select 3 mm in thickness, 6 mm in radius, and 75 wt % MPs as the optimal AM configuration.

To stabilize downward motion, we introduce a supporting layer. Under a strong attractive field from the electromagnet, the AM tends to stick to the core, making downward control difficult. To counteract this effect, we add SMs with opposite polarity to generate a repulsive force. We adjust their mixing ratio and thickness to reduce their magnetic strength (fig. S4). The SMs are magnetized with their north pole aligned upward, with a radius of 7 mm, a height of 1 mm, and 50 wt % MPs. Using a larger radius relative to the AMs improves repulsive stability under lateral and angular misalignment or deformation.

Figure 2D presents quantitative results obtained using the setup shown in Fig. 2C. In this force measurement system (FMS), we mount an AM onto the test stage and applied vertical displacements ranging from −5 to 5 mm, corresponding to the actual operating range of the device. By varying the current supplied to the electromagnet positioned below, we measure the attractive and repulsive magnetic forces exerted between the electromagnet and the AM. Both attractive and repulsive forces between the AM and the electromagnet increase exponentially as their separation decreases. Excessive magnetic attraction at short distances causes the AM to adhere to the electromagnet, compromising precise actuation control. To counteract the exponential increase in repulsive force at close range, we use a supporting layer to stabilize the nonlinear magnetic response of system and enable linear displacement control.

Figure 2E shows a photograph of a working pixel and explains how displacement is defined and measured. Figure 2F compares the displacement behavior under three supporting layer configurations. Without a supporting layer (without supporting layer), the strong magnetic attraction causes the AM to adhere to the electromagnet unless a substantial repulsive force is applied, resulting in the inability to control displacement below −2 mm. When using elastomer (Dragon Skin 30) without SMs, the layer partially suppresses downward movement but fails to adequately counteract the attraction. In contrast, incorporating SMs notably improves displacement control (fig. S7). The repulsive force increases with proximity, effectively balancing the magnetic attraction and enabling smooth and continuous modulation of pixel height across the operating range. Accordingly, pixel height can be modulated from −5 to 3.5 mm by varying the applied voltage from −20 to 30 V.

Fast, reversible, and continuous shape morphing

The proposed metasurface enables real-time shape morphing by individually controlling the vertical displacement of each pixel. Magnetic interactions between the embedded magnets and the underlying electromagnet array allow for rapid, contactless actuation. The system offers key advantages including fast response (delay time, 8 ms; rise time, 24 ms; settling time, 12 ms; movie S9), pixel-level programmability, reversible deformation, continuous operation, and low power consumption (6 W/pixel at maximum displacement), making it suitable for interactive tasks requiring reliable and dynamic surface transformation (fig. S8 and table S2).

Figure 3A shows that the proposed metasurface performs fast and reversible shape morphing through a sequence of distinct deformation modes. We conduct experiments using 3 by 3 and 6 by 6 pixel arrays, with each set of experimental images paired with corresponding finite element method (FEM) simulation results. The metasurface successfully executes four dynamic modes—oscillating, checkered, moving, and wave—in a continuous sequence (fig. S9 and movie S1). Each transition proceeds smoothly, and the FEM simulations closely match the experimentally observed deformations. These results confirm that the

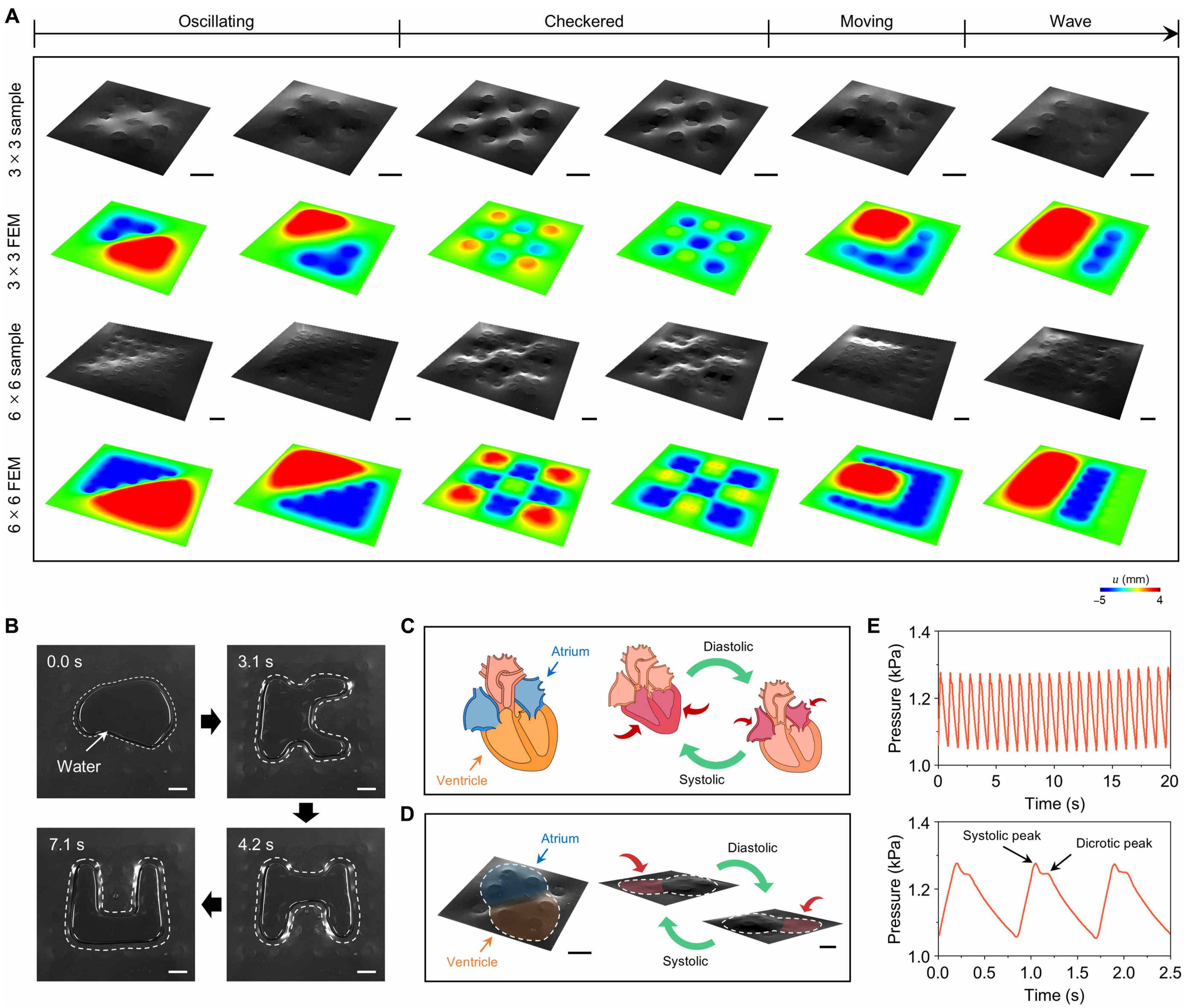

Fig. 3. Continuous and reversible shape morphing of the metasurface. (**A**) Sequential morphing of 3 by 3 and 6 by 6 metasurfaces into oscillating, checkered, moving, and wave patterns, validated by FEM. Scale bar, 20 mm. (**B**) Demonstration of droplet translation to spell "KHU" using programmed actuation. Scale bar, 20 mm. (**C**) Schematic illustration of the diastolic-systolic cycle between the atrium and ventricle in human heart. (**D**) Bioinspired demonstration mimicking the diastolic-systolic pattern, where the metasurface exhibits continuous pumping motion between the atrium (blue color) and ventricle (orange color). Scale bar, 10 mm. (**E**) Periodic pressure measured from surface deformation during the mimicking diastolic-systolic pattern of the metasurface. (Created using Blender by G.C., J.Y., and Y.P., Kyung Hee University.)

metasurface rapidly and reliably forms complex dynamic configurations across a wide range of response speeds, without mechanical delay or failure.

To verify the mechanical reliability of the shape transitions, we simulated each configuration using FEM, as shown in fig. S10. For each case, we visualize the deformed geometry, maximum surface strain distribution, and corresponding von Mises stress in the structure. The results show that surface strain remains below 30%, and the induced stress stays within the material's yield strength. These findings confirm that the metasurface preserves structural integrity and operates reversibly under repeated, continuous use.

Figure 3B demonstrates the metasurface's ability to transport objects by dynamically reshaping the surface (movie S2). A small volume of water is dispersed onto the 6 by 6 metasurface and programming vertical displacement of each individual pixel. By dynamically reconfiguring its surface topology, the metasurface effectively guided the fluid to form clearly distinguishable letters K, H, and U within 3 s, respectively. This sequence shows that the metasurface manipulates and repositions liquids by actively controlling the local topography.

Figure 3C illustrates a bioinspired model that mimics the diastolic-systolic cycle of the human heart. During a typical 1-s cardiac cycle, the diastolic phase involves a decrease in atrial volume and an increase in ventricular volume, while the systolic phase reverses this pattern, forming a continuous, repeating loop. To mimic the diastolic-systolic cycle of the heart, we divide the 3 by 3 metasurface into two regions and program it to reproduce pulsative patterns representative of cardiac activity. Figure 3D shows the experimental demonstration, where the metasurface undergoes continuous deformation in response to periodic magnetic actuation, reversibly mimicking the diastolic-systolic motion of the atrium (blue) and ventricle (orange).

Figure 3E presents time-series pressure data collected using an FMS (F105, Mark-10) during cyclic metasurface deformation. The measured signal represents superficial pressure on the metasurface and reveals key morphological characteristics of the cardiac cycle through its waveform (movie S3). The waveform shows a prominent systolic-like peak, followed by a distinct notch, closely resembling patterns observed in physiological aortic pressure profiles. These signal features, including the dicrotic notch, are widely recognized as indicators of ventricular ejection and aortic valve closure in cardiovascular waveforms (*28*). This morphological similarity demonstrates that the metasurface can emulate complex, nature-inspired dynamic behaviors, enabling users to perceive rhythmic sensations accompanied by emotional feedback during interaction (fig. S11). It replicates not only biologically inspired shapes but also realistic temporal actuation profiles under rapid, repetitive, and thermally stable long-term operation (fig. S12). The system can achieve up to 10^{30} discrete shape reconfigurations, estimated from the combinatorial configuration of bidirectional actuation and aspect ratio per pixel, highlighting its vast reconfigurability potential (*3*).

Self-sensing surface reconstruction using embedded IMU sensors

To reconstruct the surface shape of the metasurface in real time without external equipment such as depth cameras, we directly integrate IMU sensors onto the actuating layer. Each IMU measures the local surface tilt at its location, and these angular values are used to compute the overall surface profile. Figure 4A illustrates the arrangement of IMU sensors on a 3 by 3 metasurface and the geometric principle used to convert the measured roll and pitch angles into vertical displacement. Given the distance (l) between two adjacent AMs and the tilt angle (θ) measured by the IMU positioned between them, the total height difference ($u_i + u_j$) can be calculated (fig. S13 and text S2). Using this method with six IMU sensors, the heights of all nine AMs are reconstructed to obtain the complete surface profile.

To generate a continuous surface map from the discrete AM heights, we apply a Gaussian-weighted interpolation defined by the following equation

$$z(x,y) = \sum_{i=1}^{9} z_i \cdot \exp\left(- \frac{(x-xi)^2 + (y-yi)^2}{2\sigma^2} \right) \tag{1}$$

Here, z_i represents the calculated height of each AM at position (x_i, y_i), and σ is a tunable parameter that controls the spatial smoothness of the interpolation. We adjust σ to minimize the error between the interpolated surface and the depth camera measurements. Figure S14 shows the relationship between σ and the mean reconstruction error. On the basis of this analysis, we select σ value of 11.5, which yields the lowest discrepancy between the IMU-based reconstruction and the surface profile measured by the depth camera.

To evaluate the real-time sensing performance of the IMUs, we programmed the metasurface to perform continuous wave–like motion and selected one of the six IMU sensors to record roll and pitch angles over time. Figure 4B shows the temporal variation of both angles, exhibiting a periodic trend that matches the programmed motion. These results confirm that the embedded IMU sensors accurately capture the dynamic tilt of the surface during continuous operation.

To verify the accuracy of the reconstructed surface shape, we compare the IMU-based cross-sectional profile with the one measured by a depth camera under identical conditions. Figure 4C presents the displacement curves obtained from both methods, exhibiting strong agreement. This demonstrates that the IMU-derived reconstruction reliably reflects the actual surface deformation with high accuracy.

Figure 4D summarizes the static reconstruction results for four different surface configurations (demos 1 to 4). For each case, we show the input voltage pattern, a photograph of the deformed surface, the corresponding FEM simulations, surface profiles measured by a depth camera and IMU mapping, and the error distribution between the two. The error follows a Gaussian distribution centered near zero, indicating that the IMU-based measurement maintains high accuracy across varying conditions. In addition, fig. S15 shows a spatial error map based on the depth camera measurements, revealing that most regions remain within ± 2 mm error.

These findings demonstrate that the metasurface can accurately monitor and reconstruct its own surface shape in real time without external vision systems. Embedded IMU sensors enable precise tracking of surface motion, facilitating closed-loop feedback and adaptive control. Furthermore, by increasing IMU density and refining the system with a kinematic model to address complex deformations, even large-scale surface changes can be effectively detected (*29*). This capability establishes the system as a highly scalable, self-sensing, and programmable platform for dynamic surface modulation.

Human-machine interaction enabled by softness and magnetic actuation

The proposed metasurface is composed of soft silicone-based materials and operates through remotely controlled magnetic forces, allowing it to withstand direct physical contact without structural damage. This combination of compliant materials and noncontact

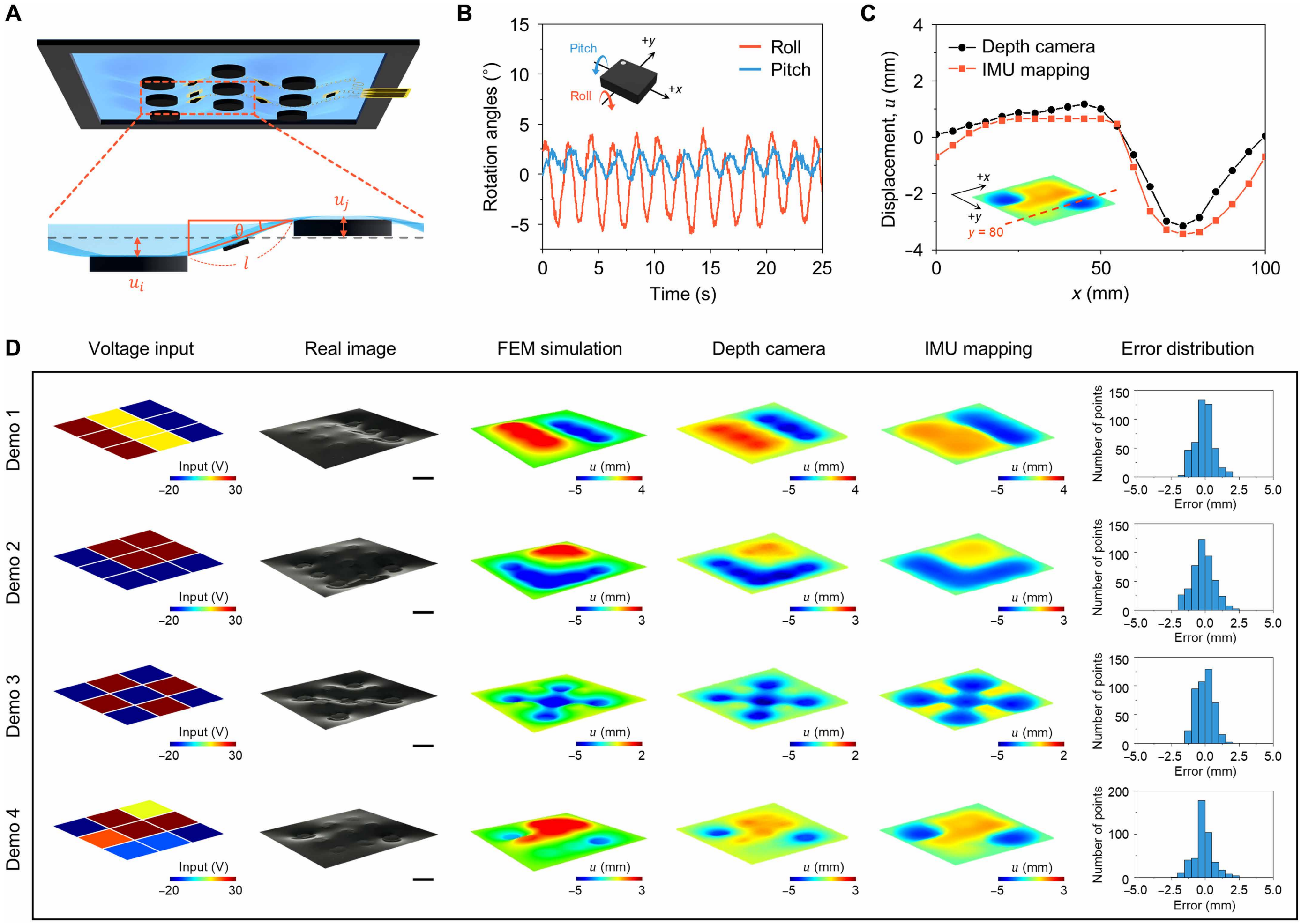

Fig. 4. Real-time surface shape reconstruction using embedded IMU sensors. (**A**) Concept of height reconstruction from local tilt angles measured by six IMU sensors embedded on a 3 by 3 metasurface. (**B**) Time series of roll and pitch angles during dynamic wave motion. (**C**) Cross-sectional surface profile comparison between depth camera measurement and IMU-based reconstruction. (**D**) Four static demos showing voltage input, real shape, FEM prediction, depth camera result, IMU-based reconstruction, and error distribution. Scale bars, 20 mm. (Created using Blender by G.C., J.Y., and Y.P., Kyung Hee University.)

actuation enables reliable recovery and safe interaction with human users, establishing the system as a promising platform for intuitive human-machine interfaces.

Figure 5A illustrates the reconfiguration process, which integrates an inverse design strategy with a multiphysics finite element modeling framework and IMU-based feedback. Electromagnetic and mechanical coupling among electromagnets and elastomeric layers governs the metasurface deformation. Because of the nonlinear and configuration-dependent nature of magnetic forces, simplified displacement-voltage models are inadequate for accurate shape control. To address this, the inverse design strategy uses a semianalytical approach based on the work-reciprocity principle and is verified against representative 3D FEM force-displacement predictions to generate initial voltage inputs without running additional FEM simulations (text S3 and fig. S16), thereby reducing convergence time in the IMU-based feedback loop. Experimental force-displacement data calibrate and validate the semianalytical predictions. Experimental force-displacement data calibrate and validate the FEM predictions.

For a given target shape, simulations compute the required magnetic forces to achieve a desired height ($F_i^{\text{target}} \rightarrow z_i^{\text{target}}$), which are then mapped to voltages via calibrated force-displacement curves (Fig. 2D), enabling rapid and accurate actuation. The initial voltage values obtained from the inverse design model are applied to each electromagnet array. An IMU mapping system attached to the surface collects tilt data at each node, which is then used to reconstruct the actual displacement (z_i^{real}) of the AMs in three dimensions. The mean squared error (MSE; e) is subsequently calculated on the basis of the difference between the actual displacement and the target height value (z_i^{target}). If the MSE exceeds a predefined threshold ($e \geq 1$), then the voltage is updated for each AMs based on the displacement error ($\Delta z_i = z_i^{\text{target}} - z_i^{\text{real}}$). The updated magnitude is determined by multiplying the error by a gain factor (η), which is experimentally set to 0.8 (fig. S17). The updated voltages are reapplied to the electromagnet array, and the IMU system measures the resulting surface state to perform real-time displacement error analysis. This process is repeated until the error converges to an acceptable level

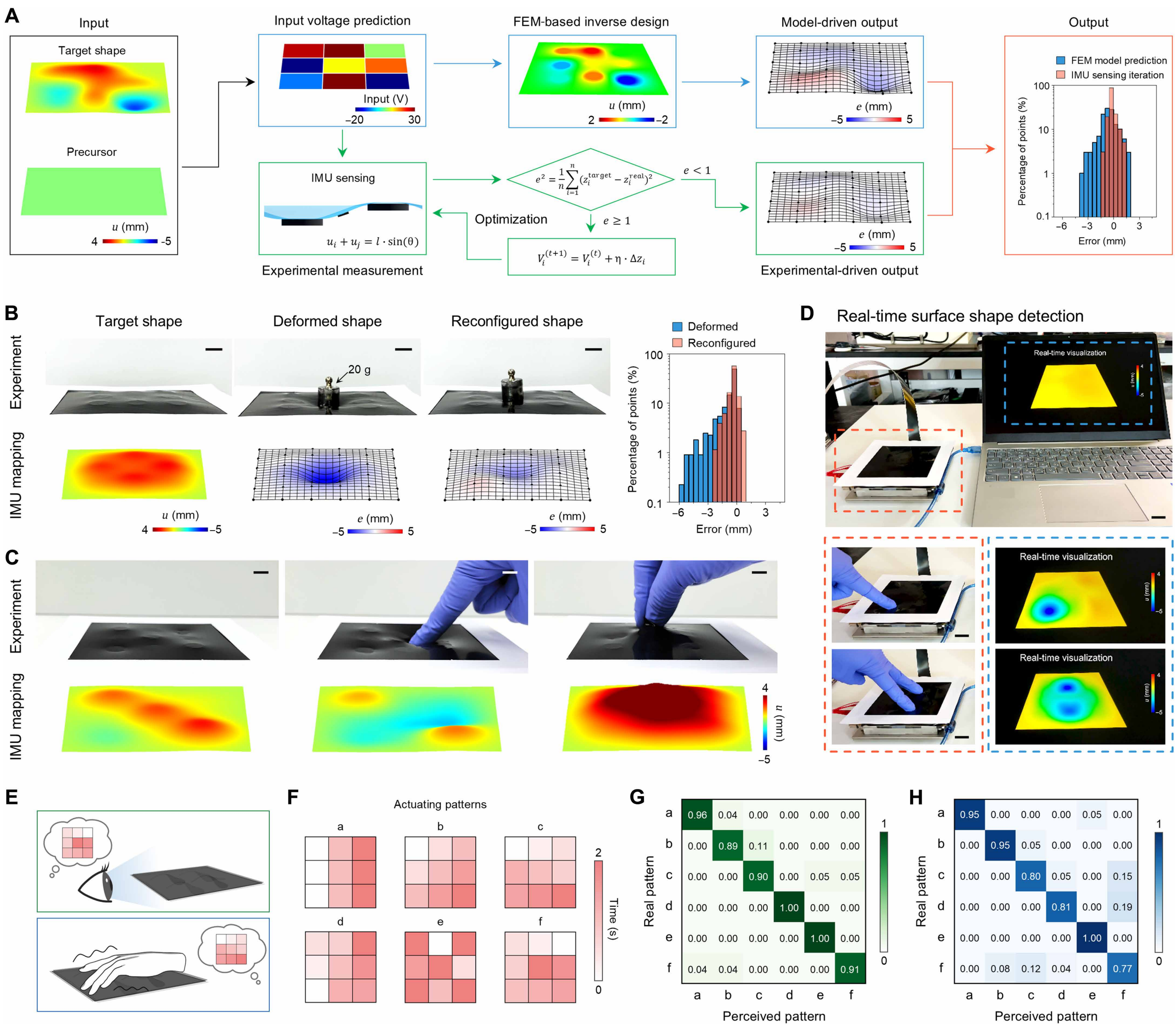

Fig. 5. Human interaction and self-recovery of the metasurface. (**A**) Flow diagram of the inverse design approach based on a FEM calculations (blue) and the experiment-driven self-reconfiguration process implemented using IMU-based imaging feedback and an error function–based optimization algorithm (green). (**B**) Surface reconfiguration under external loading: adaptation from deformed to target shape with reduced error. Scale bars, 10 mm. (**C**) Surface response to pressing and pinching during wave motion with real-time IMU-based height mapping. Scale bars, 10 mm. (**D**) Real-time visualization of surface deformation through IMU sensing and external display. Scale bars, 20 mm. (**E**) Schematic illustration of the perception test evaluating whether users can visually or tactilely perceive shape changes of the metasurface. (**F**) Six actuating patterns applied to the 3 by 3 metasurface used in the perception test, each presented to users in a randomized order. (**G** and **H**) Confusion matrix of perception test results (10 participants, $n = 30$ trials per pattern) comparing perceived patterns with actual actuating patterns at visually (G) and tactilely (H) (*$P < 0.001$). (Created using Blender by G.C., J.Y., and Y.P., Kyung Hee University.)

($e < 1$), enabling the surface to progressively approach the target shape. After reconfiguration, the error distribution shifts toward zero, substantially reducing displacement errors. As a result, the metasurface closely matches the intended target shape with high fidelity.

Building on this recovery behavior, we evaluate whether the metasurface can actively restore its shape by adjusting the actuation input in response to external loads. As shown in Fig. 5B, application of a 20-g weight to a predefined target shape induces undesired deformation. Subsequent tuning of the input voltages enables the system to reconfigure and closely restore the original surface profile. Visual comparisons and error distributions indicate that the reconfigured shape yields negligible error, with a Gaussian-like distribution centered near zero. These results demonstrate the system's ability to compensate for deformation through controlled magnetic reprogramming (fig. S18).

To demonstrate resilience during active operation, we manually perturb the metasurface while performing a wave-like motion.

Figure 5C shows that the surface quickly returns to its original shape after being pressed or pinched by a hand and continues its motion without interruption (movie S4). IMU-based height maps capture both the temporary deformation and the recovery, confirming that the system preserves mechanical functionality through the elasticity of its structure and the reversibility of magnetic actuation. Furthermore, this performance remained consistent even after 5000 cycles of repeated testing (fig. S19).

The metasurface also enables real-time sensing and visualization of user interaction. Figure 5D illustrates that the embedded IMU sensors immediately detect local tilt upon surface contact and transmit the reconstructed shape to a connected monitor (movie S5). This capability provides instant visual feedback, reinforcing the system's role as a responsive and interactive platform.

To evaluate whether the shape transformations of the metasurface are perceived consistently during user interaction, we evaluate its ability to provide both visual and tactile feedback. Figure 5E illustrates the perception test used to determine whether users can recognize shape changes visually or tactilely. The visual test is conducted at a distance of 30 cm, while the tactile test involves placing the metasurface directly against the user's palm. Six distinct actuation patterns are applied to the 3 by 3 metasurface and presented in randomized order during user interaction (Fig. 5F).

Figures 5 (G and H) presents the results of the perception tests comparing the actuation patterns perceived by users with the actual actuation patterns of the metasurface under visual and tactile conditions. Confusion matrices based on responses from 10 adult participants (table S1) indicate a highest accuracy of agreement between the perceived and actual patterns. These results demonstrate that users can reliably perceive the intended shape transformations of the metasurface through both visual and tactile feedback. This capability reinforces the system's potential as a practical, responsive, and interactive platform for real-world applications.

Together, the findings confirm that the metasurface resists physical disturbances, autonomously restores its shape, adapts to external inputs, and responds to human interaction in real time. These integrated capabilities make it well suited for soft, wearable, and tactile-responsive human-machine interface applications.

Integration of LED array for 3D shape–responsive display

To expand the functionality of the metasurface beyond shape morphing, a 7 by 7 RGB (red-green-blue) LED array is integrated directly onto the actuating layer to create a dynamic, shape-responsive 3D display. This integration allows the system not only to transform physically but also to visually communicate its topography in real time.

Figure 6A shows an exploded view of the enhanced actuating layer, which integrates the RGB LED array, IMU sensor circuit, AMs, and flexible elastomeric substrate. The embedded IMU sensors capture the overall surface morphology, from which the height at each of the 49 surface-integrated LED positions is estimated. The LEDs are individually controlled to display distinct colors, providing a visual representation of the 3D surface profile.

Figure 6B demonstrates the LED array accurately reflects topographical changes based on IMU data (fig. S20 and movie S6). In the flat state, the LEDs display a uniform green color. Upon surface indentation, the corresponding region turns blue, reflecting reduced height sensed by the IMUs. Programmed deformations induced by magnetic inputs generate a color gradient aligned with a colormap (movie S7). A side-by-side comparison confirms strong agreement between the LED visualization and IMU-based height mapping, demonstrating real-time surface feedback. To demonstrate the expressive potential of the platform, we simulate natural phenomena by combining surface motion with dynamic lighting effects. In Fig. 6C, a paper boat is placed on the metasurface, which is actuated to generate wave-like deformations simulating ocean motion. The surface profile is synchronized with a color shift from white to blue to represent cresting waves, creating a visually compelling maritime navigational scene. Figure 6D presents a ripple effect, in which the center of the metasurface rises and propagates outward, mimicking the impact of a water droplet. The deformation is animated in coordination with surface color transitions to visually represent the spreading motion of the ripples (movie S8).

These demonstrations establish a programmable 3D display that integrates tactile shape transformation with real-time visual output. The system emulates natural motions and visually enriched interactions, paving the way for future applications in interactive displays, tangible media, and bioinspired communication interfaces.

DISCUSSION

This study presents a magnetically actuated soft mechanical metasurface capable of continuous and reversible shape morphing, along with integrated real-time sensing and visual feedback. By embedding composite magnetic structures within elastomeric layers, the system achieves spatially programmable deformation while maintaining mechanical compliance and structural resilience.

The proposed architecture overcomes several limitations of conventional shape-morphing systems. The dual-magnet configuration, which separates upward and downward actuation, enables stable and precise displacement control at the pixel level. Unlike previous systems that are either vulnerable to physical contact or excessively rigid because of the use of stiff materials, the metasurface presented in this study features a fully soft front layer and operates in a programmable manner through remote magnetic control. The magnetic actuation provides fast response in a contactless mode, allowing rapid deformation cycles and dynamic surface reprogramming.

Notably, the metasurface can be grasped or twisted by hand and still fully restore its original shape and function without structural damage. It is a mechanically reconfigurable metasurface capable of maintaining both structural recoverability and continuous operation even after direct human interaction. In contrast to pneumatic or thermally responsive systems, the proposed design does not rely on external bulky components or slow actuation processes, thereby minimizing fatigue accumulation during repeated operation. The simple structure and high responsiveness of this system facilitate large-area scalability and the integration of multimodal stimuli, suggesting its potential for future multifunctional platforms such as human-machine interfaces and tactile feedback displays.

In addition to mechanical robustness, the system features real-time shape reconstruction through embedded IMU sensors. This sensing approach eliminates the need for external imaging systems such as depth cameras, which often become inoperable during active user interaction. The sensors continuously track deformation and allow real-time surface reconstruction, enabling feedback-driven operation. Furthermore, a 7 by 7 RGB LED array integrated into the surface provides height-dependent color output, allowing the metasurface to function as a 3D display that responds visually to its own shape state. By replicating dynamic motions such as waves and ripples and synchronizing these with visual signals, the system exhibits behavior

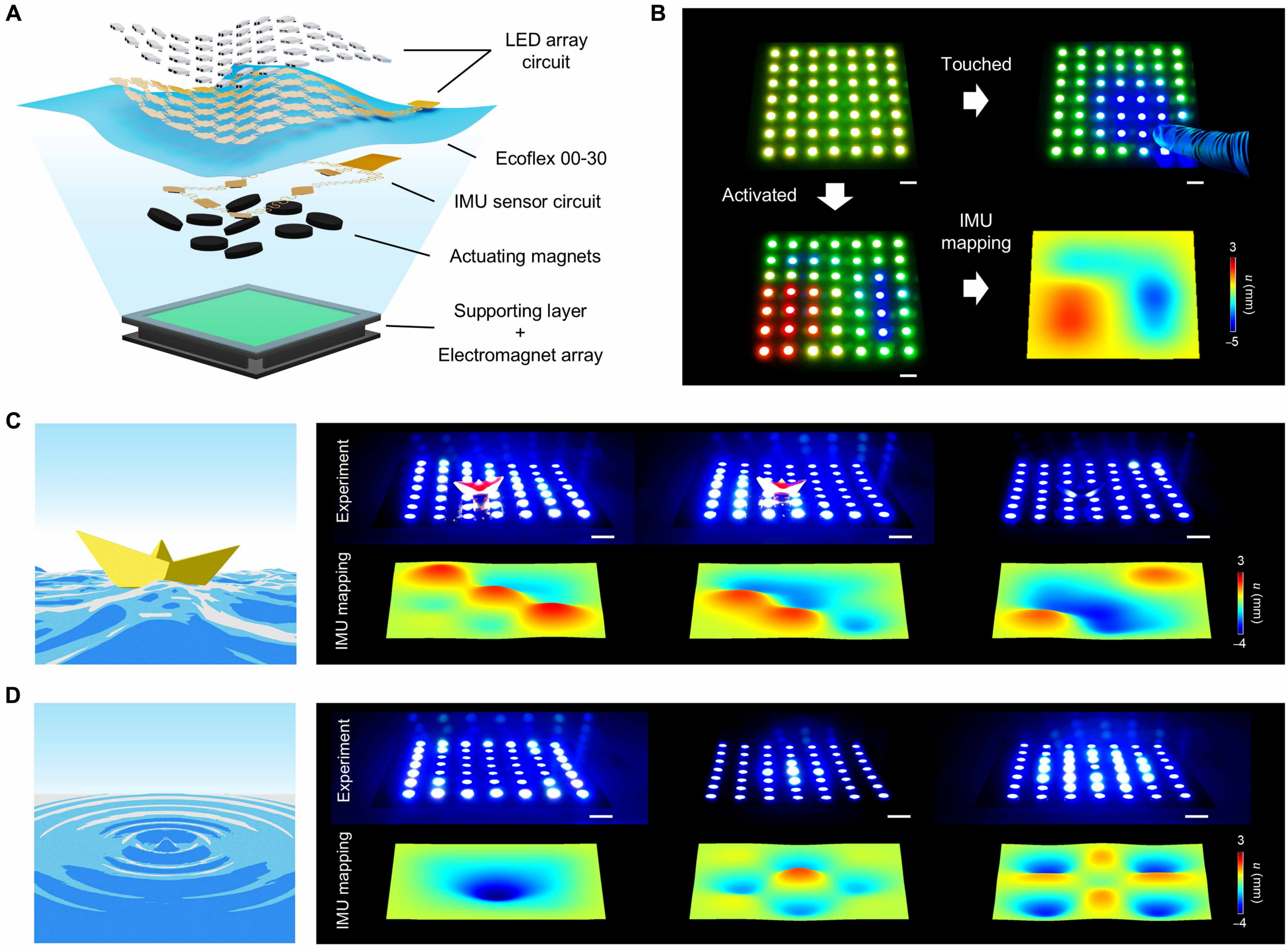

Fig. 6. Surface-integrated LED visualization and 3D display capability. (**A**) Exploded view of the actuating layer with integrated RGB LED array and IMU sensors. (**B**) Real-time height-to-color mapping of surface deformation visualized on the LED array. (**C**) Demonstration of a paper boat responding to programmed wave motion and color modulation. (**D**) Ripple effect simulated through concentric deformation and LED-based color gradients. Scale bars, 10 mm. (Created using Blender by G.C., J.Y., and Y.P., Kyung Hee University.)

that parallels certain biological surfaces. It adapts to external forces, detects and processes local deformation, and conveys shape information through embedded visual output. These features reflect the essential characteristics of bioinspired interfaces that respond to both environmental and user-driven input.

In summary, we present a multifunctional soft metasurface that integrates programmable actuation, self-sensing, and real-time visualization. Its ability to intuitively interact with humans without functional compromise highlights its potential as a next-generation human-machine interactive interface capable of conveying diverse tactile cues, including temperature (joule heater), vibration (eccentric rotating mass actuator), humidity (hydrogel and humidity module), and surface texture.

MATERIALS AND METHODS

Device fabrication

The actuating layer was fabricated by mixing parts A and B of Ecoflex 00-30 (Smooth-On) in a 1:1 weight ratio, followed by vacuum degassing. The mixture was cast into a mold and cured at room temperature for 24 hours to form a 300-μm-thick sheet. AMs were prepared by mixing PDMS base and curing agent (Sylgard 184, Dow) at a 10:1 weight ratio, followed by the addition of NdFeB MPs at a 3:1 weight ratio relative to PDMS. The mixture was poured into a mold and cured at 70°C for 2 hours, producing cylindrical magnets (radius, 6 mm; height, 3 mm). The magnets were magnetized under a 2-T field using an electromagnet (KR TECH) and bonded to the Ecoflex sheet with silicone adhesive (Sil-Poxy, Smooth-On). The assembled layer was prestretched by 10% along both axes and fixed to an acrylic frame.

The supporting layer was formed from Dragon Skin 30 (Smooth-On), mixed in a 1:1 ratio, and cured at room temperature to a thickness of 500 μm. SMs were fabricated by mixing PDMS and NdFeB MPs at a 1:1 weight ratio and cast and cured using the same procedure. Cylindrical magnets (radius, 7 mm; height, 1 mm) were magnetized and attached to the Dragon Skin 30 sheet using Sil-Poxy. The layer was prestretched by 10% before frame mounting.

An array of 20 mm–by–15 mm electromagnets (LS-P2015, JKemc; 5- to 24-V dc, 0.1 to 0.22 A, 29.4-N holding force) was assembled with stainless steel housings in an $N \times M$ configuration. Each electromagnet was connected to an H-bridge motor driver (L298N, LC Technology) for polarity control and driven via pulse-width modulation using a pulse width modulation (PWM) driver (PCA9685, Adafruit). Communication and signal routing were managed by an Arduino Uno and an 8-bit shift register (SN74HC595, Texas Instruments) via I^2C protocol.

IMU sensor circuit fabrication

A sacrificial poly(methyl methacrylate) (PMMA) layer (495 A8, Microresist; 0.08 μm) was spin coated onto a silicon wafer at 4000 rpm for 40 s and cured at 180°C for 30 s. A polyamic acid solution (Sigma-Aldrich) was then spin-coated at 1500 rpm for 40 s and thermally cured at 150°C for 30 min, 200°C for 30 min, and 250°C for 1 hour to yield a 3.75-μm-thick polyimide (PI) layer. Cr/Au (10 nm/300 nm) was deposited via thermal evaporation to form electrode traces and patterned by lift-off. A second 3.75-μm PI layer was spin coated and cured using the same conditions to encapsulate the metal. A Cu hard mask was then formed and patterned by lift-off. Contact pads and outline geometries were defined by photolithography and etched by O_2 plasma reactive ion etching. The entire device was released by dissolving the PMMA sacrificial layer in acetone and transferred onto water-soluble tape (ASWT-2, Aquasol). IMU chips (LSM6DSL, STMicroelectronics) were manually aligned and soldered onto the flexible circuit using low-temperature solder paste (SMDLTLFPT6, Chip Quik) and bonded with a heat gun for integration into the elastomeric structure.

LED circuit fabrication

The LED circuit was designed using electronic design automation software (EAGLE, Autodesk) and fabricated on flexible printed circuit boards by an external manufacturer (PCBWay). Surface-mounted addressable RGB LEDs (WS2812B) were manually aligned and soldered onto the flexible printed circuit boards (fPCBs) using low-temperature solder paste (SMDLTLFPT6, Chip Quik), followed by bonding with a heat gun. The completed LED layer was integrated into the elastomeric metasurface structure.

Finite element modeling (mechanical-magnetic) of metasurface deformation

A 3D coupled mechanical-magnetic FEM framework was developed to predict the nonlinear deformation behavior of the magnetic metasurface in response to spatially varying voltage inputs from electromagnets. The magnetic force was first quantified using COMSOL Multiphysics (version 6.2) with the Magnetic Fields, No Currents module. A 3D model of the permanent PDMS-NdFeB magnets (radius, 6 mm; height, 3 mm) and electromagnets (AM: radius, 6 mm; height, 3 mm; SM: radius, 7 mm; height, 1 mm) was constructed and simulated in an air domain to compute the resulting magnetic field and force exerted on the magnet. To ensure numerical accuracy of the magnetic field solution and force calculation, an infinite element domain was used to model the air boundary (outer radius, 2500 mm), and a fine mesh was implemented with element sizes equal to one-eighth of the permanent magnet thickness. The total number of elements in the simulation was ~1,281,000. The remanent magnetic flux density in the thickness direction (B_z) was set to 147.9 mT for the AM and 23.7 mT for the SM based on experimentally measured material-specific magnetization properties from the weight % of magnetic MPs. For the electromagnet, a linear magnetization–voltage scaling relationship is assumed as $B_E = K\phi$, where $K = 12.5$ mT/V is an experimentally determined constant from the surface magnetic field measurements. This constant K captures the combined effects of the coil geometry, turn density, and magnetic susceptibility. The variable ϕ is the applied voltage. A parametric sweep was performed to compute the magnetic force F_m as a function of the magnet-electromagnet separation distance, ranging from −5 to 5 mm. The resulting force values were compared to the elastic restoring force of the membrane to assess the equilibrium condition required for voltage actuation.

Mechanical simulations were then performed using the commercial software ABAQUS 2023. A 3D deformable model of the metasurface was constructed to simulate target shape morphing and to quantify the resulting displacement and strain fields across the soft structure. The 300-μm metasurface (Ecoflex 00-30) and 500-μm supporting layer (Dragon Skin 30) were modeled using four-node reduced integration shell elements (S4R), while the embedded PDMS-NdFeB magnets were modeled with eight-node hybrid 3D solid elements (C3D8RH) to accurately capture large deformations and near-incompressibility. The total number of elements in the mechanical simulation is ~75,000. A mesh convergence study was conducted to ensure accuracy. The PDMS-NdFeB magnets were modeled using a nearly incompressible linear elastic material model with a Young's modulus of $E_{magnet} = 1.8$ MPa and Poisson's ratio of $\nu_{magnet} = 0.49$. The metasurface and supporting layers were modeled as nearly incompressible hyperelastic Mooney-Rivlin solids. For Ecoflex 00-30, the material constants were $C_{10} = 0.013$ MPa, $C_{01} = 0.003$ MPa, and $D = 1.25$ MPa^{-1}. For Dragon Skin 30, the material constants were $C_{10} = 0.050$ MPa, $C_{01} = 0.012$ MPa, and $D = 0.32$ MPa^{-1}. A 10% biaxial prestretch was applied to the metasurface, consistent with the experimental fabrication process, before the application of the electromagnetic forces.

Characterization

Magnetic field strength was measured using a Gauss meter (GS-100D2, LANDTEK). Magnetic hysteresis curves of the composite magnets were obtained with a vibrating sample magnetometer (Microsense). Surface deformation was captured using a depth camera (POP 3, Revopoint 3D) and reconstructed as 3D models with Blender software. Magnetic interaction forces were measured using an FMS (F105, Mark-10). AMs were mounted on the test stage and displaced vertically from −5 to 5 mm to match the operational range of the device. At each position, the input current to the underlying electromagnet was adjusted, and the corresponding attractive or repulsive force was recorded.

Evaluation of visual and tactile perception of shape transformations

Ten adult participants (four males and six females; age range, 20 to 27 years; mean age, 22.1 years; SD, 2.5 years) participated in the perception experiments. The experiment consisted of two perception tasks designed to assess recognition of shape transformations rendered by a programmable 3 by 3 metasurface array. Under the visual condition, the metasurface was positioned 30 cm in front of the participant, who was instructed to observe the shape changes without physical contact. Under the tactile condition, participants rested their palm directly on top of the device while blindfolded to eliminate visual input. Six distinct actuation patterns, generated by selectively activating different subsets of units within the array, were used in both conditions.

Six distinct actuation patterns, generated by selectively activating different subsets of units within the array, were used under both conditions. In each modality, each of the six patterns was presented to every participant three times in a randomized order, resulting in a total of 18 trials per participant (30 trials per pattern across all participants). Before the main trials, participants were given the opportunity to practice two randomly selected patterns to ensure task familiarity. During the test, participants were asked to identify the perceived pattern by selecting from a set of six predefined options. All responses were recorded immediately after each trial.

Supplementary Materials

The PDF file includes:
Supplementary Text S1 to S4
Figs. S1 to S22
Tables S1 and S2
Legends for movies S1 to S9

Other Supplementary Material for this manuscript includes the following:
Movies S1 to S9

REFERENCES

1. A. Walther, From responsive to adaptive and interactive materials and materials systems: A roadmap. *Adv. Mater.* **32**, e1905111 (2020).
2. D. Shah, B. Yang, S. Kriegman, M. Levin, J. Bongard, R. Kramer-Bottiglio, Shape changing robots: Bioinspiration, simulation, and physical realization. *Adv. Mater.* **33**, e2002882 (2021).
3. J. Wang, A. Chortos, Performance metrics for shape-morphing devices. *Nat. Rev. Mater.* **9**, 738–751 (2024).
4. T. Y. K. Ankit, A. Ho, M. R. Nirmal, D. Kulkarni, N. Accoto, Mathews, Soft actuator materials for electrically driven haptic interfaces. *Adv. Intell. Syst.* **4**, 2100061 (2022).
5. A. Rafsanjani, K. Bertoldi, A. R. Studart, Programming soft robots with flexible mechanical metamaterials. *Sci. Robot.* **4**, eaav7874 (2019).
6. M. Li, A. Pal, A. Aghakhani, A. Pena-Francesch, M. Sitti, Soft actuators for real-world applications. *Nat. Rev. Mater.* **7**, 235–249 (2022).
7. L. Hines, K. Petersen, G. Z. Lum, M. Sitti, Soft actuators for small-scale robotics. *Adv. Mater.* **29**, 1603483 (2017).
8. S. An, X. Li, Z. Guo, Y. Huang, Y. Zhang, H. Jiang, Energy-efficient dynamic 3D metasurfaces via spatiotemporal jamming interleaved assemblies for tactile interfaces. *Nat. Commun.* **15**, 7340 (2024).
9. Y. Qiu, Z. Lu, Q. Pei, Refreshable tactile display based on a bistable electroactive polymer and a stretchable serpentine joule heating electrode. *ACS Appl. Mater. Interfaces* **10**, 24807–24815 (2018).
10. I. Hwang, S. Mun, J.-H. Youn, H. J. Kim, S. K. Park, M. Choi, T. J. Kang, Q. Pei, S. Yun, Height-renderable morphable tactile display enabled by programmable modulation of local stiffness in photothermally active polymer. *Nat. Commun.* **15**, 2554 (2024).
11. A. M. Rauf, J. S. Bernardo, S. Follmer, in *2023 IEEE International Conference on Robotics and Automation (ICRA)* (IEEE, 2023), pp. 2591–2597.
12. B. Johnson, M. Naris, V. Sundaram, A. Volchko, K. Ly, S. Mitchell, E. Acome, N. Kellaris, C. Keplinger, N. Correll, A multifunctional soft robotic shape display with high-speed actuation, sensing, and control. *Nat. Commun.* **14**, 4516 (2023).
13. T. Wang, J. Zhang, J. Hong, M. Y. Wang, Dielectric elastomer actuators for soft wave-handling systems. *Soft Robot.* **4**, 61–69 (2017).
14. E. Hajiesmaili, D. R. Clarke, Reconfigurable shape-morphing dielectric elastomers using spatially varying electric fields. *Nat. Commun.* **10**, 183 (2019).
15. S. Gallo, C. Son, H. J. Lee, H. Bleuler, I.-J. Cho, A flexible multimodal tactile display for delivering shape and material information. *Sens. Actuators A Phys.* **236**, 180–189 (2015).
16. J. Tsimeris, C. Dedman, M. Broughton, T. Gedeon, in *Proceedings of the 2013 ACM International Conference on Interactive Tabletops and Surfaces* (Association for Computing Machinery, 2013), pp. 175–178.
17. K. Liu, F. Hacker, C. Daraio, Robotic surfaces with reversible, spatiotemporal control for shape morphing and object manipulation. *Sci. Robot.* **6**, eabf5116 (2021).
18. H. Yang, X. Yin, C. Zhang, B. Chen, P. Sun, Y. Xu, Weaving liquid crystal elastomer fiber actuators for multifunctional soft robotics. *Sci. Adv.* **11**, eads3058 (2025).
19. D. Hwang, E. J. Barron III, A. T. Haque, M. D. Bartlett, Shape morphing mechanical metamaterials through reversible plasticity. *Sci. Robot.* **7**, eabg2171 (2022).
20. G. Risso, M. Kudisch, P. Ermanni, C. Daraio, Tuning the properties of multi-stable structures post-fabrication via the two-way shape memory polymer effect. *Adv. Sci.* **11**, e2308903 (2024).
21. S. Oh, S. Lee, S. H. Byun, S. Lee, C. Y. Kim, J. Yea, S. Chung, S. Li, K. I. Jang, J. Kang, J.-W. Jeong, 3D shape-morphing display enabled by electrothermally responsive, stiffness-tunable liquid metal platform with stretchable electroluminescent device. *Adv. Funct. Mater.* **33**, 2214766 (2023).
22. M. J. Ford, C. P. Ambulo, T. A. Kent, E. J. Markvicka, C. Pan, J. Malen, T. H. Ware, C. Majidi, A multifunctional shape-morphing elastomer with liquid metal inclusions. *Proc. Natl. Acad. Sci. U.S.A.* **116**, 21438–21444 (2019).
23. X. Ni, H. Luan, J.-T. Kim, S. I. Rogge, Y. Bai, J. W. Kwak, S. Liu, D. S. Yang, S. Li, S. Li, Z. Li, Y. Zhang, C. Wu, X. Ni, Y. Huang, H. Wang, J. A. Rogers, Soft shape-programmable surfaces by fast electromagnetic actuation of liquid metal networks. *Nat. Commun.* **13**, 5576 (2022).
24. Y. Bai, H. Wang, Y. Xue, Y. Pan, J.-T. Kim, X. Ni, T.-L. Liu, Y. Yang, M. Han, Y. Huang, A dynamically reprogrammable surface with self-evolving shape morphing. *Nature* **609**, 701–708 (2022).
25. J. Wang, M. Sotzing, M. Lee, A. Chortos, Passively addressed robotic morphing surface (PARMS) based on machine learning. *Sci. Adv.* **9**, eadg8019 (2023).
26. J. Yoo, G. Chung, Y. Park, Bio-inspired, miniaturized magnetic heart valve system for superior performance cardiovascular simulator. *Adv. Mater.* **37**, e2419504 (2025).
27. J. Kim, J. Yoo, H. Seo, R. Avila, G. Chung, G. Shin, S. Gwak, Y. Han, J.-H. Lee, H.-J. Yoon, Y. Park, Magnetically driven triboelectric nanogenerator for a wireless, versatile energy transfer system. *Sci. Adv.* **11**, eadu5919 (2025).
28. W. W. Nichols, M. F. O'Rourke, McDonald's blood flow in arteries: Theoretical, experimental and clinical principles, W. W. Nichols, M. F. O'Rourke, E. R. Edelman, C. Vlachopoulos, Eds. (CRC Press, London, ed. 3, 1990)
29. Z. Zhou, P. Chen, Y. Lu, Q. Cui, D. Pan, Y. Liu, J. Li, Y. Zhang, Y. Tao, X. Liu, L. Sun, G. Wang, 3D deformation capture via a configurable self-sensing IMU sensor network. *Proc. ACM Interact. Mobile Wearable Ubiquitous Technol.* **7**, 1–24 (2023).

Acknowledgments
Funding: This work was supported by the National Research Foundation of Korea (NRF) grant funded by the Korea government (MSIT) (RS-2023-00211261 and RS-2025-02309992). Y.P. acknowledged support from the Korea Research Institute of Chemical Technology (KRICT) through KS2621-40. R.A. acknowledges support from the Rice ENRICH Office and the seed grant from the Rice Space Institute. **Author contributions:** G.C., J.Y., P.L., R.A., and Y.P. conceived the overall research goals and aims. G.C., J.Y., P.L., G.S., D.J., S.L., R.A., and Y.P. performed the designs, engineering investigation, and manufacturing for the devices. G.C., J.Y., and Y.P. performed data analysis and device performance testing. G.C., J.Y., and J.-Y.Y. performed the design and fabrication of the fPCB. P.L. and R.A. performed mechanical simulation analysis of the devices. G.C., J.Y., P.L., R.A., and Y.P. performed the construction of the FEA-based self-reconfiguration algorithm. G.C., J.Y., P.L., R.A., and Y.P. were responsible for the original drafting of the manuscript. G.C., J.Y., P.L., G.S., D.J., S.L., J.-Y.Y., S.M.W., D.-S.H., J.-H.K., W.S., R.A., and Y.P. assisted in critical editing and review of the final manuscript. **Competing interests:** The authors declare that they have no competing interests. **Data, code, and materials availability:** All data and code needed to evaluate and reproduce the results in the paper are present in the paper and/or the Supplementary Materials. This study did not generate new materials.

Submitted 2 February 2026
Accepted 12 May 2026
Published 26 June 2026
10.1126/sciadv.aeg0480

Science Advances

Magnetically levitated metasurface enabling tangible and bidirectional human-machine interaction

Gooyoon Chung, Jeongmin Yoo, Pei Liu, Gyuri Shin, Dongkyu Jeong, Sunjin Lee, Jae-Young Yoo, Sang Min Won, Dong-Soo Han, Ji-Hoon Kim, Wooseok Song, Raudel Avila, and Yoonseok Park

Sci. Adv. **12** (26), eaeg0480. DOI: 10.1126/sciadv.aeg0480

Science Advances (ISSN 2375-2548) is published by the American Association for the Advancement of Science. 1200 New York Avenue NW, Washington, DC 20005. The title *Science Advances* is a registered trademark of AAAS.